

# Wall treatment of multiple correction k-exact schemes

A. Menasria<sup>\*,\*\*</sup>, P. Brenner<sup>\*</sup> and P. Cinnella<sup>\*\*</sup>  
Corresponding author: amandine.menasria@laposte.net

<sup>\*</sup> Ariane Group, France.

<sup>\*\*</sup> Arts et Métiers ParisTech, DynFluid laboratory, France.

**Abstract:** A  $k^{\text{th}}$ -order accurate wall treatment is investigated for high-order Godunov-type finite volume schemes based on  $k$ -exact polynomial reconstructions in each cell of the primitive variables via a successive corrections procedure of the derivatives. We focus more specifically on the 1-exact and 2-exact schemes, which offer a good trade-off between accuracy and computational efficiency. In both cases, the reconstruction stencil is modified at the boundaries. Additionally, information about wall curvature is taken into account by introducing bicubic Bézier patches for the reconstruction of the wall faces. The benefits of the proposed numerical treatments are shown up for two inviscid cases, namely the flow past a Gaussian bump and the subsonic flow around a circular cylinder.

*Keywords:* Computational Fluid Dynamics, Finite volumes, High-order methods,  $k$ -exact reconstruction, Curvature, Bicubic Bézier patches, Low-Mach-number flows.

## 1 Introduction

In the context of Computational Fluid Dynamics, high-order finite volume schemes are praised for their ability to provide high-fidelity solutions of challenging configurations including for example flow unsteadiness, boundary layers separation or steep gradients.

A widely studied family of high-order schemes, initially introduced by Barth and Frederickson [1, 2] and Vandersbilck and Deconinck [3], is represented by the so-called  $k$ -exact schemes. These combine high-order piecewise polynomial reconstructions of the solution and its derivatives over mesh cells and high-order formulae for the calculation of flux integrals [4, 5, 6, 7]. In previous work [6, 8, 7], an efficient successive-corrections procedure for computing high-order approximations of the solution and its successive derivatives was introduced and assessed against several steady and unsteady flow configurations [7], showing its capability of ensuring high-order accuracy on fully unstructured grids.

However, for practical reasons, the reconstruction stencil is simplified at solid walls. Moreover, the wall surface is approximated with polygonal faces, introducing a spatial error of order  $\mathcal{O}(h^2)$ ,  $h$  being the mesh size [9]. These two features can prevent the scheme to reach its nominal order of accuracy in certain flow configurations with critical wall phenomena or with curved boundaries [10].

Additionally, near-wall flow regions, which are characterized by strong gradients (boundary layers, shock/boundary layer interactions, heat transfer), exhibit low local values of the Reynolds and Mach numbers. A degradation of the accuracy of Reynolds Averaged Navier-Stokes (RANS) method has been observed for low-Mach configurations [11] due to the inability of compressible solvers to reproduce flows in the incompressible limit [11].

In the aim of progressing toward a more accurate representation of wall bounded flow configurations with curved boundaries, an improved wall treatment is investigated in the present paper. Firstly, a high-order composite representation of the wall with bicubic Bézier patches [12, 13, 14] is added to the solver and employed to calculate the geometrical moments required to integrate the fluxes in our methodology. Secondly, a low-Mach correction is introduced to recenter the upwind scheme in near-wall region, thus improving the

accuracy in the incompressible limit. Thirdly, a methodology for enriching the reconstruction stencil in the vicinity of solid walls consistently with the existing scheme is proposed.

The present developments are implemented within the industrial code FLUSEPA<sup>1</sup>, developed by the European aerospace company Ariane Group to model all the phases of flight of a space launcher such as takeoff, stage separation, and reentry [15]. The solver can simulate tridimensional, unsteady, compressible, viscous and reactive flows loaded with particles over bodies in relative motion. A CHIMERA-like strategy based on 3D intersections coupled with an Adaptive Mesh Refinement module [16] is used to deal with complex geometries.

This article is organized as follow. In Section 2, the baseline spatial solver implemented in FLUSEPA is recalled. In Section 3, the surface model chosen to account for boundary curvature and its implementation within the solver are described. A low-Mach recentering model is proposed and explained in Section 4. Near-wall discretization is investigated in Section 5. Numerical validations on selected inviscid and viscous cases are presented and discussed in Section 6. Conclusions and perspectives for future work are made in Section 7.

## 2 Numerical scheme

In this Section, the current-point spatial discretization schemes [6, 7] are recalled in the inviscid flow case. Let  $q(\mathbf{x}, t)$  be a variable verifying a set of conservation equations of the form

$$\frac{\partial q}{\partial t} + \vec{\nabla} \cdot \mathbf{F} = 0. \quad (1)$$

where  $\mathbf{F}$  denotes the flux function of  $q$ .

Following a cell-centered finite volume approach, the domain is divided into  $N$  non-overlapping cells  $(\Omega_J)_{J \in [1, N]}$  of volume  $|\Omega_J|$  and cell center  $\mathbf{x}_j = \frac{1}{|\Omega_J|} \iint_{\Omega_J} \mathbf{x} dV$ . The computational variables are the averaged values

$$\bar{q}_J = \frac{1}{|\Omega_J|} \iiint_{\Omega_J} q dV. \quad (2)$$

Integration of Eq. (1) on  $\Omega_J$  and application of Gauss' theorem yields

$$|\Omega_J| \frac{d\bar{q}_J}{dt} + \sum_{K=1}^P \iint_{A_{JK}} \mathbf{F}(q) \cdot \mathbf{n} dS \quad (3)$$

with  $A_{JK}$  the interface between cell  $J$  and its neighbour  $K$ ,  $P$  the total number of neighbours of  $J$  and  $\mathbf{n}$  the local outward-pointing normal.

The solver consists in three steps, following the pattern of  $k$ -exact schemes [1, 2]:

- Reconstruction of the solution in each cell;
- Flux integration along the faces;
- Advance in time.

Two temporal schemes are implemented for time discretization in the code. The first one is an explicit second-order Heun scheme with consistent local time stepping [17]. The second one is an implicit scheme of order 1 used in combination with an iterative Generalized Minimal Residual Method (GMRES) [18] to solve the linear system along with a Newton algorithm for convergence. Advance in time is not detailed any further since it would be beyond the scope of the present paper (see [8] for more details).

---

<sup>1</sup>Registered trademark in France with number 134009261

## 2.1 Solution reconstruction

To reconstruct the solution in a given cell  $\Omega_J$  to the  $k^{th}$  order, a Taylor expansion of order  $k$  at the cell centroid  $\mathbf{x}_j$  is performed. For a third-order reconstruction

$$q(\mathbf{x}) = q_j + \mathbf{D}^{(1)}q_j \cdot (\mathbf{x} - \mathbf{x}_j) + \frac{1}{2}\mathbf{D}^{(2)}q_j \bullet [(\mathbf{x} - \mathbf{x}_j) \otimes (\mathbf{x} - \mathbf{x}_j)] + \mathcal{O}(h^3) \quad (4)$$

with  $\mathbf{D}^{(1)}q$  and  $\mathbf{D}^{(2)}q$  the gradient vector and the second derivatives tensor of  $q$ . Index  $j$  refers to pointwise value at  $\mathbf{x}_j$ .  $\bullet$  is the contracted product and  $\otimes$  is the tensor product.

A classical method to determine a reconstruction is to solve the system of Eq. (4) such that the derivatives verify conservativity relations in a least-squares sense [19, 20]. Such method has the drawback to be sensitive to mesh irregularities [21].

The reconstruction procedure used in this work is described below. In the following, call  $s(J)$  the direct neighbourhood of cell  $\Omega_J$ , comprising the cells  $\Omega_K$  that share a common edge with  $\Omega_J$ , and  $\Omega_J$  itself.

### 2.1.1 Linear reconstruction of the solution

For a second-order accurate reconstruction, we need to calculate  $q_j$  at second order and  $\mathbf{D}^{(1)}q_j$  at first order. For this purpose we construct a 1-exact reconstruction operator for the gradient  $\mathcal{D}_1^{(1)}[\bar{q}]_J$ . In this notation:

- the italic font means that the function is a linear approximation operator;
- the index letter refers to the reconstruction stencil. Here it is  $J$ , hence the operator is defined on  $s(J)$ ;
- $\bar{q} = (\bar{q}_{K \in s(J)})$  are the averaged variables of the conservative variables on the stencil  $s(J)$ . The left and right brackets in  $[\bar{q}]$  means that the gradient is constructed as a function of these variables;
- the exponent refers to the derivation order. Here the operator approximates the first derivatives (solution gradient);
- the index number refers to the accuracy order. Here we are looking for a 1-exact [7] operator on  $s(J)$ , *i.e.* such that

$$\forall \mathbf{x} \in s(J), \mathcal{D}_1^{(1)}[\bar{q}]_J(\mathbf{x}) = \mathbf{D}^{(1)}q(\mathbf{x}) + \mathcal{O}(h). \quad (5)$$

In the solver, the reconstruction is applied to the primitive variables because it is a more robust choice than to apply it to the conservative ones. For each primitive variable  $q$ , an average  $\bar{q}$  is defined, which can be expressed as a function of the averaged conservative variables. Reconstruction of  $\bar{q}$  from the conservative variables in the  $k$ -exact framework is described in [7]. For a second-order accurate reconstruction, we want

$$\bar{q} = \tilde{q} + \mathcal{O}(h^2). \quad (6)$$

which is directly obtained by definition of  $\tilde{q}$ .

To compute the gradient, a technique based on a modification of the Green-Gauss method is used [7, 8]. Gauss' theorem is applied to the exact gradient to bring back the problem to the calculation of surface integrals, which are then approximated with a linear interpolation between the left and right averaged cells values.

$$\frac{1}{|\Omega_J|} \iiint_{\Omega_J} \mathbf{D}^{(1)}q(\mathbf{x})dV = \frac{1}{|\Omega_J|} \sum_{K=1}^P \iint_{A_{JK}} q \mathbf{n} dS = \mathbf{D}^{(1)}q(\mathbf{x}_j) + \mathcal{O}(h) \quad (7)$$

$$\iint_{A_{JK}} q \mathbf{n} dS = (\beta_K \bar{q}_K + (1 - \beta_K) \bar{q}_J) \mathbf{A}_{JK}, \text{ with } \beta_K = \frac{\|\mathbf{x}_j - \mathbf{x}_\Gamma\|}{\|\mathbf{x}_j - \mathbf{x}_\Gamma\| + \|\mathbf{x}_k - \mathbf{x}_\Gamma\|} \in [0, 1] \quad (8)$$

with  $\mathbf{A}_{JK} = \mathcal{O}(h^2)\mathbf{n}_{JK}$  the surface vector of interface  $A_{JK}$ ,  $|\Omega_J| = \mathcal{O}(h^3)$  the volume of cell  $J$ , and  $\mathbf{x}_\Gamma$  a chosen point related to the interface called integration point. The choice of such a point will be discussed in Section 3. Eq. (8) is not used for wall faces: the original solver sets  $\beta_K = 0$  for these faces such that the

contribution of the wall is totally excluded from the reconstruction stencil. This will be modified in Section 5.

The preceding approximation is not 1-exact for all meshes and may become inconsistent for strongly deformed grids. A 1-exact gradient operator should satisfy the conditions

$$\begin{cases} \sum_{K \in s(J)} \mathbf{W}_{JK} = \mathbf{0} \text{ (0-exactness)} \\ \sum_{K \in s(J)} (\boldsymbol{\alpha} \cdot (\mathbf{x}_K - \mathbf{x}_J)) \mathbf{W}_{JK} = \boldsymbol{\alpha} \text{ (1-exactness)}. \end{cases} \quad (9)$$

where  $(\mathbf{W}_{JK})_{K \in s(J)}$  are weight vectors such that  $\mathcal{D}_1^{(1)}[\bar{q}]_J = \sum_{K \in s(J)} \mathbf{W}_{JK} \bar{q}_K$ .

To construct the 1-exact gradient, we use a correction procedure, starting from a 0-exact approximation obtained by combining Eqs. (7) and (8):

$$\mathcal{D}_0^{(1)}[\bar{q}]_J = \frac{1}{|\Omega_J|} \sum_{K \in s(J)} (\beta_K \bar{q}_K + (1 - \beta_K) \bar{q}_J) \mathbf{A}_{JK} \quad (10)$$

To recover consistency on general unstructured grids, a corrective operator is built, with associated matrix  $M_1(J)$ . The latter is called the simple correction matrix [8]. The correction matrix  $M_1(J)$  for the linear operator (10) is obtained by applying the conditions (9) to the canonical basis of the polynomials of degree 1  $(x - x_j, y - y_j, z - z_j)$ . This gives

$$M_1(J) \mathcal{D}_1^{(1)}[\bar{q}]_J = \mathcal{D}_0^{(1)}[\bar{q}]_J \quad (11)$$

This leads to the so-called Quasi-Green 1-exact gradient operator

$$\mathcal{D}_1^{(1)}[\bar{q}]_J = M_1^{-1}(J) \frac{1}{|\Omega_J|} \sum_{K \in s(J)} (\beta_K \bar{q}_K + (1 - \beta_K) \bar{q}_J) \mathbf{A}_{JK}, \text{ with } M_1(J) = \sum_{K \in s(J)} \beta_K \mathbf{A}_{JK} \otimes (\mathbf{x}_K - \mathbf{x}_J) \quad (12)$$

with  $M_1^{-1}(J)$  the inverse of matrix  $M_1(J)$ . Note that for cartesian meshes,  $M_1(J)$  is the identity matrix. This procedure corresponds to a second-order accurate representation of the variable.

### 2.1.2 Parabolic reconstruction of the solution

For a third-order accurate reconstruction we need to calculate  $q_j$  at third order,  $\mathcal{D}^{(1)}q_j$  at second order and  $\mathcal{D}^{(2)}q_j$  at first order.

First, the primitive averaged values  $\bar{q}$  must be computed to the third-order. A correction term  $\Delta q$  is established using what has been done in part 2.1.1: details of this procedure can be found in [7].

Then, successive corrections of the derivatives are carried out. The 1-exact gradient operator (12) is composed with itself, leading to an inconsistent approximation of the second derivatives in  $\mathbf{x}_j$

$$\mathcal{D}_0^{(2)}[\bar{q}]_J = \mathcal{D}_1^{(1)} \left[ \mathcal{D}_1^{(1)}[\bar{q}]_J \right]_K \quad (13)$$

The consistency of the second-order derivatives approximate is restored on general meshes using the linearity properties of the operator (13) and 2-exactness constraints (see [22]). This gives a third-order tensor  $M_2(J)$ , which depends on geometrical quantities of two levels of neighbours of cell  $J$  (neighbours of  $J$  and their neighbours).

$$\mathcal{D}_1^{(2)}[\bar{q}]_J = M_2(J)^{-1} \mathcal{D}_0^{(2)}[\bar{q}]_J \quad (14)$$

We then correct the 1-exact approximation gradient to increase its accuracy to the second order, by calculating the truncation error between the exact gradient and its 1-exact reconstruction operator. For each component  $m \in \{1, 3\}$  of the gradient, a geometrical matrix  $H_1(J)_m$  is calculated, which depends only on quantities of the cells of the direct neighbourhood  $s(J)$ :

$$(\mathcal{D}^{(1)}q_j)_m = \overbrace{(\mathcal{D}_1^{(1)}[\bar{q}]_J)_m - \mathcal{D}^{(2)}q_j \bullet H_1(J)_m}^{(\mathcal{D}_2^{(1)}[\bar{q}]_J)_m} + \mathcal{O}(h^2) \quad (15)$$

with  $\mathcal{D}^{(2)}q_j$  given by Eq. (14). This procedure leads to a third-order polynomial of the variable.

## 2.2 Flux integration

Flux integration along face  $A_{JK}$  is achieved by using a one-point integration formula, based on a Taylor expansion to the third order:

$$\iint_{A_{JK}} \mathbf{F} \cdot \mathbf{n} dS = \mathbf{F}_{|\Gamma} \cdot \mathcal{S}_{A_{JK}}^{(0)} + \mathcal{D}^{(1)}\mathbf{F}_{|\Gamma} \cdot \mathcal{S}_{A_{JK}}^{(1)} + \frac{1}{2}\mathcal{D}^{(2)}\mathbf{F}_{|\Gamma} \bullet \mathcal{S}_{A_{JK}}^{(2)} + \mathcal{O}(h^3)\mathbf{A}_{JK} \quad (16)$$

where  $\mathbf{x}_{\Gamma}$  is the integration point and where  $\mathcal{S}_{A_{JK}}^{(m)}$  are the surface moments of order  $m$  of the interface  $A_{JK}$

$$\mathcal{S}_{A_{JK}}^{(m)} = \iint_{A_{JK}} (\mathbf{x} - \mathbf{x}_{\Gamma})^{\otimes m} \mathbf{n} dS, \quad m \in \{0, 1, 2\}; \quad (17)$$

Surface moments are tensors of order  $m$  which are fundamental to the solver and should size in  $\mathcal{O}(h^m)$ . Calculating these quantities and the location of the integration point in order to reflect accurately the shape of the boundary when curvature is present is the object of Section 3. Note that Eq. (16) is different from the classical choice of Gauss points to integrate fluxes.

For a third-order reconstruction process, we need  $\mathbf{F}_{|\Gamma}$  at order 3,  $\mathcal{D}^{(1)}\mathbf{F}_{|\Gamma}$  at order 2 and  $\mathcal{D}^{(2)}\mathbf{F}_{|\Gamma}$  at order 1.

These approximations are obtained by solving a Riemann problem at the interface  $A_{JK}$ . Left and right values of the variable are given by the solution reconstruction and derivative approximates established previously, following a MUSCL-type approach [23].

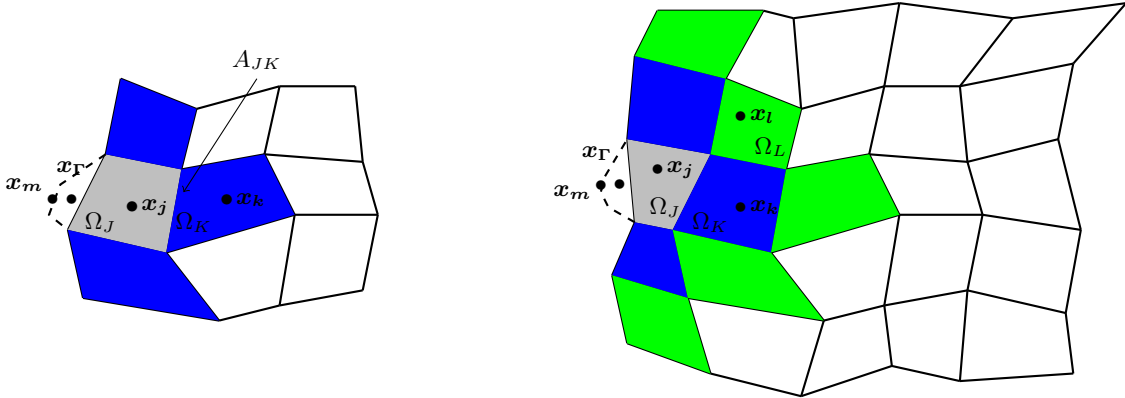


Figure 1: Discretization stencil at the wall and curved wall face for the: (a) 1-exact reconstruction scheme; (b) 2-exact reconstruction scheme.

## 3 Wall curvature

Taking into account the wall curvature is essential for high-order boundary treatment. In the baseline implementation of FLUSEPA, boundary faces are represented by flat faces<sup>2</sup>, introducing a second-order spatial error compared to the actual surface [9]. However, the approximation of the physical surface has to be at least of the order of the numerical scheme to ensure the nominal order of accuracy close to the wall

<sup>2</sup>More precisely, triangular faces are used. Quadrangular faces are treated by being split into two triangles.

[10]. In the case of parametric surfaces using a polynomial basis, and for a third-order accurate scheme, the polynomials have to be at least of degree two.

For this purpose, we use the geometric module BSHAPE developed by INRIA [14], which generates from a surface mesh a composite surface made of bicubic Bézier patches.

A bicubic Bézier patch is a parametric polynomial surface of degree three originated by De Casteljau and Bézier [12] around the same time. Given a set of 16 control points  $(\mathbf{P}_{ij})_{i \in \{0,1,2,3\}, j \in \{0,1,2,3\}}$ , the equation of the Bézier patch is given by  $\mathbf{f}(u \in [0, 1], v \in [0, 1]) = \sum_{i=0}^3 \sum_{j=0}^3 B_i^3(u) B_j^3(v) \mathbf{P}_{ij}$ , where  $(B_k^3)_{k \in \{0,3\}}$  are the Bernstein polynomials of degree three [13].

BSHAPE module is based on a point normal interpolation meshing strategy [24]: the patches are generated with the points coordinates and associated normals of the mesh. The model ensures G1 continuity, *i.e.* tangent plane continuity, between the patches.

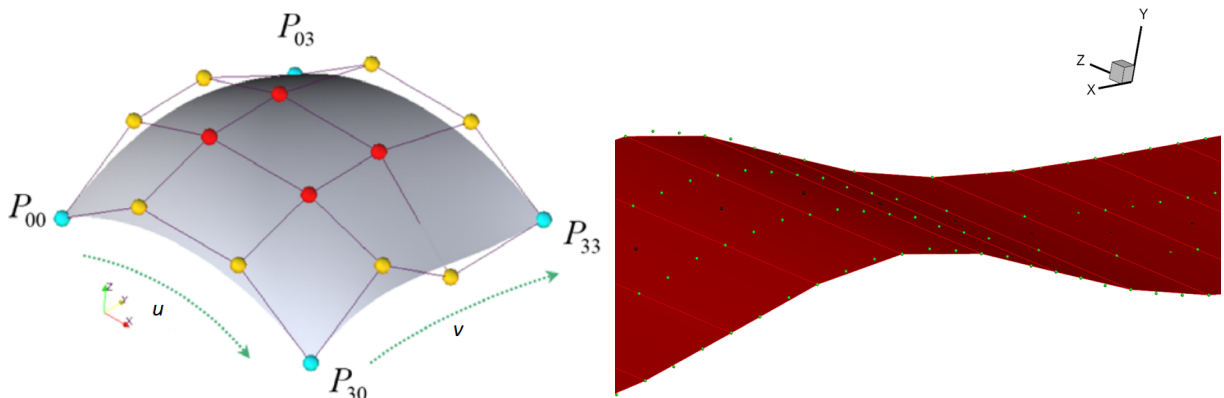


Figure 2: (a) Representation of a Bézier patch; (b) Control points  $(\mathbf{P}_{i,j})_{i \in \{0,1,2,3\}, j \in \{0,1,2,3\}}$  and middle point  $\mathbf{x}_m$  generated by the solver for the wall faces of the bump test case

The module has been incorporated in FLUSEPA. The geometry routine selects the wall faces and the side faces sharing an edge with the wall faces, and generates a set of control points corresponding to a patch for each wall face (see Figure 2). The composite surface is not directly seen by the solver, that is, a new mesh is not created, but the information about the patches, namely the control points, is used to integrate the boundary geometric quantities required for the scheme introduced in Section 2. The surface moments of the wall faces are derived by integrating analytically the constitutive equation of the patch. Then volume moments and centroids of the boundary cells are deduced by the application of Gauss' theorem.

This strategy was tested on simple configurations for which the analytical equation of the surface is known, such as a parabolic channel and a sphere. Geometrical moments of order 0 (cell volume), 1 and 2 were calculated and a decrease of the geometrical error from 1 up to 2 orders of accuracy was observed.

In addition to computing more accurately the geometrical quantities, flux integration on curved wall faces needs further modifications.

In the original solver, the integration point  $\mathbf{x}_\Gamma$  is constructed to minimize the first-order error in the flux integration:  $\mathbf{x}_\Gamma$  is chosen so that the associated surface moments of order 1 are orthogonal to  $\mathbf{A}_{JK}$ . Consequently, the first-order error in the normal face direction  $\mathbf{n}_{JK} = \frac{\mathbf{A}_{JK}}{\|\mathbf{A}_{JK}\|}$  cancels out by construction.

$$\mathbf{x}_\Gamma = \begin{pmatrix} \frac{1}{\|\mathbf{A}_{JK}\|} \left( \iint_{A_{JK}} x \mathbf{n} dS \right) \cdot \mathbf{n}_{JK} \\ \frac{1}{\|\mathbf{A}_{JK}\|} \left( \iint_{A_{JK}} y \mathbf{n} dS \right) \cdot \mathbf{n}_{JK} \\ \frac{1}{\|\mathbf{A}_{JK}\|} \left( \iint_{A_{JK}} z \mathbf{n} dS \right) \cdot \mathbf{n}_{JK} \end{pmatrix} \quad (18)$$

In case of a flat face,  $\mathbf{n}$  is constant equal to  $\mathbf{n}_{JK}$  thus  $\mathbf{x}_\Gamma$  is the center of gravity of the face and lies on the face. However, when the face is curved,  $\mathbf{n}$  is not constant:  $\mathbf{x}_\Gamma$  is not equal a priori to the center of gravity of the face. More importantly, it does generally not lie on the face.

In case of a curved wall, flux and its derivatives needed in Eq. (16) are evaluated at a particular point of the patch. In a first approach, the middle point of the patch  $\mathbf{x}_m$  is chosen (point of the patch with parameters  $u = 0.5$  and  $v = 0.5$ ). This is not a problem for the error generated during the flux integration, as long as the flux and its derivatives are approximated to the required order of accuracy. Concerning the resolution of the Riemann problem at the wall, the local normal at point  $\mathbf{x}_m$  is used instead of the integrated normal  $\mathbf{n}_{JK}$ .

The radius of curvature is also computed for each patch and will be used in Section 5 for the pressure boundary condition. In two-dimensional space, any twice differentiable curve can be locally approximated by a circular arc whose radius is called the radius of curvature. In three-dimensional space, several types of curvatures can be defined. In the present work, we consider the normal curvature associated to a given direction. The tangential velocity (generally non-zero for Euler cases) is calculated at the middle point of the patch, and the radius of curvature  $R$  associated to this vector and to the normal at this point is estimated (see Chapter 19 of [13]).

## 4 Low-Mach recentering

Boundary layers being characterized by low-speed flow, constructing a compressible scheme accurate at low-Mach numbers appears as an important condition to deal with complex wall phenomena. In a pioneering article, Volpe [25] investigated the performances of compressible codes at very low-Mach numbers and observed that some of the codes suffered from a lack of accuracy in the low-Mach regime.

Some specific spatial configurations are exempted from this accuracy problem. Non-linear Godunov-type schemes do not exhibit low-Mach inaccuracy on  $1D$  grids, and on  $2D$  (resp.  $3D$ ) grids with triangular (resp. tetrahedral) cells [26, 27, 28]. Such a result is however only proved for periodic or unbounded spatial domains [26].

By adimensionalizing the Euler equations with two different time scales and expanding the variables in power of the Mach number, two limit solutions are deduced for low-speed flows [29]: an incompressible one and an acoustic one which corresponds to fluctuations of the flow. These limits are both physically relevant and generally coexist.

Guillard and Viozat [30] and Guillard and Murrone [31] showed, by means of asymptotic analysis, that the order of the pressure fluctuations are responsible for the limit to which the solution of the scheme will converge to :

$$\begin{cases} P = P_0 + \mathcal{O}(M^2) & \text{in the incompressible limit} \\ P = P_0 + \mathcal{O}(M) & \text{in the acoustic limit} \end{cases} \quad (19)$$

Rieper [32] pointed out that a too important normal jump of velocity in the Riemann problem at cell interfaces leads to an incorrect pressure scaling.

A review of the main strategies to address the low-Mach problem for compressible flows is given in [29]. The goal of all these curative solutions is to remove the acoustic perturbations. Preconditioning techniques, initially inspired by Turkel's approach [33] are used to derive initial data that permit to recover a correct scaling of the pressure fluctuations, as given in Eq. (19) [32, 31, 30, 34].

In the present work, a low-Mach recentering approach is chosen, which consists in adapting the numerical viscosity of the scheme to suppress the unwanted acoustic part of the solution. This procedure is justified by a physical approach in the next Section.

### 4.1 Derivation of the recentering functions on pressure and velocity for a Godunov-type Riemann solver

In this Section, a linearized version of the governing equations is considered as a prototype for investigating the behaviour of numerical schemes in the low-Mach number limit and developing suitable corrections for our Riemann solver.

In the low-Mach regime, the non-linear part of the Riemann solver is negligible compared to its linear part. We can thus study the linearized Euler equations along with a linear Riemann solver to understand the low-Mach problem.

To simplify the demonstration, we consider the isentropic Euler equations, for which the pressure is a single-valued function of the density

$$\begin{cases} \frac{\partial \rho}{\partial t} + \vec{\nabla} \cdot (\rho \mathbf{u}) = 0 \\ \frac{\partial \mathbf{u}}{\partial t} + \mathbf{div}(\rho \mathbf{u} \otimes \mathbf{u}) + \vec{\nabla} P = \mathbf{0} \end{cases} \quad (20)$$

and inject first-order perturbations of a steady flow  $\rho = \rho_0 + \rho'$ ,  $\mathbf{u} = \mathbf{u}_0 + \mathbf{u}'$  and  $P = P_0 + c^2 \rho'$  into Eqs. (20),  $c$  being the speed of sound. This yields to the linearized Euler equations:

$$\begin{cases} \frac{\partial P'}{\partial t} + \mathbf{u}_0 \cdot \vec{\nabla} P' + \rho_0 c^2 \vec{\nabla} \cdot \mathbf{u}' = 0 \\ \frac{\partial \mathbf{u}'}{\partial t} + \overline{\mathbf{grad}}(\mathbf{u}') \mathbf{u}_0 + \frac{1}{\rho_0} \vec{\nabla} P' = \mathbf{0} \end{cases} \quad (21)$$

In the following, the prime symbol will be dropped to alleviate the notations. Eqs. (21) are then integrated on  $\Omega_J$  in a finite volume approach, and Green-Gauss theorem is applied:

$$\begin{cases} |\Omega_J| \frac{d\overline{P}_J}{dt} + \sum_K (\mathbf{u}_0 \cdot \mathbf{S}_{JK}) P_\Gamma + \rho_0 c^2 \sum_K \mathbf{u}_\Gamma \cdot \mathbf{S}_{JK} = 0 \\ |\Omega_J| \frac{d\overline{\mathbf{u}}_J}{dt} + \sum_K (\mathbf{u}_0 \cdot \mathbf{S}_{JK}) \mathbf{u}_\Gamma + \frac{1}{\rho_0} \sum_K P_\Gamma \mathbf{S}_{JK} = \mathbf{0} \end{cases} \quad (22)$$

where  $P_\Gamma$  and  $\mathbf{u}_\Gamma$  are the pressure and velocity values at the interface point  $\mathbf{x}_\Gamma$ . For simplicity, we assume that time integration is performed using the first-order forward Euler scheme. Then the system (22) can be written again as

$$\begin{cases} \overline{P}_J^{n+1} = \overline{P}_J^n - \frac{\Delta t}{|\Omega_J|} \sum_K (\mathbf{u}_0 \cdot \mathbf{S}_{JK}) P_\Gamma^n - \rho_0 c^2 \frac{\Delta t}{|\Omega_J|} \sum_K \mathbf{u}_\Gamma^n \cdot \mathbf{S}_{JK} \\ \overline{\mathbf{u}}_J^{n+1} = \overline{\mathbf{u}}_J^n - \frac{\Delta t}{|\Omega_J|} \sum_K (\mathbf{u}_0 \cdot \mathbf{S}_{JK}) \mathbf{u}_\Gamma^n - \frac{\Delta t}{|\Omega_J|} \frac{1}{\rho_0} \sum_K P_\Gamma^n \mathbf{S}_{JK} \end{cases} \quad (23)$$

We denote  $M_{JK} = \frac{\mathbf{u}_0 \cdot \mathbf{n}_{JK}}{c}$  the interface Mach number in the direction normal to face  $JK$ .  $P_\Gamma^n$  and  $\mathbf{u}_\Gamma^n$  can be calculated with a classical first-order Godunov scheme [35]:

If  $|M_{JK}| \geq 1$  then:

if  $M_{JK} \geq 1$  then:

$$\begin{cases} P_\Gamma^n = \overline{P}_J^n \\ \mathbf{u}_\Gamma^n = \overline{\mathbf{u}}_J^n \end{cases} \quad (24)$$

else if  $M_{JK} \leq -1$  then:

$$\begin{cases} P_\Gamma^n = \overline{P}_K^n \\ \mathbf{u}_\Gamma^n = \overline{\mathbf{u}}_K^n \end{cases} \quad (25)$$

If  $|M_{JK}| \leq 1$  then:

$$\begin{cases} P_\Gamma^n = \frac{\overline{P}_J^n + \overline{P}_K^n}{2} + \frac{\rho_0 c}{2} (\overline{\mathbf{u}}_J^n - \overline{\mathbf{u}}_K^n) \cdot \mathbf{n}_{JK} \\ \mathbf{u}_\Gamma^n = \frac{\overline{\mathbf{u}}_J^n + \overline{\mathbf{u}}_K^n}{2} + \frac{1}{2\rho_0 c} (\overline{P}_J^n - \overline{P}_K^n) \mathbf{n}_{JK} \end{cases} \quad (26)$$

In low-Mach configurations, the calculation of the interface values is close to what is done in Eqs. (26), even when a non-linear Godunov solver is used. We see that these two equations are composed of a centered term and of the equivalent of an upwind term whose role is to stabilize the solution through numerical dissipation. Consequently, the loss of accuracy observed in the incompressible limit is due to these "upwind" terms, which become too strong when the Mach number approaches to zero. This motivates the idea of recentering these terms with some recentering functions that will be noted  $\psi_{JK}^P$  for the pressure equations and  $\psi_{JK}^u$  for the velocity equation:

$$\begin{cases} P_\Gamma^n = \frac{\overline{P}_J^n + \overline{P}_K^n}{2} + \frac{\rho_0 c}{2} \psi_{JK}^P (\overline{\mathbf{u}}_J^n - \overline{\mathbf{u}}_K^n) \cdot \mathbf{n}_{JK} \\ \mathbf{u}_\Gamma^n = \frac{\overline{\mathbf{u}}_J^n + \overline{\mathbf{u}}_K^n}{2} + \frac{1}{2\rho_0 c} \psi_{JK}^u (\overline{P}_J^n - \overline{P}_K^n) \mathbf{n}_{JK} \end{cases} \quad (27)$$

Two natural conditions on the functions  $\psi_{JK}^P$  and  $\psi_{JK}^u$  can be derived from physical arguments. Firstly, the two functions must be comprised between zero and one, since their role is to decrease the upwind term without changing its sign in the normal direction  $n_{JK}$ . Secondly,  $\psi_{JK}^P$  and  $\psi_{JK}^u$  must be continuous functions of the normal Mach number  $M_{JK}$ , and they must allow to recover the classical Godunov scheme for Mach numbers greater than one:

$$\begin{cases} 0 \leq \psi_{JK}^P(M_{JK}) \leq 1 \\ 0 \leq \psi_{JK}^u(M_{JK}) \leq 1 \\ \psi_{JK}^P(M_{JK} \geq 1) = 1 \\ \psi_{JK}^u(M_{JK} \geq 1) = 1 \end{cases} \quad (28)$$

In order to find suitable expressions for  $\psi_{JK}^P$  and  $\psi_{JK}^u$ , relations (24), (25) and (27) are plugged into (22). After calculations, a linear expression valid for all Mach numbers is finally obtained:

$$\begin{cases} \overline{P_J^{n+1}} = \overline{P_J^n} - \frac{\Delta t}{2|\Omega_J|} \sum_K \alpha_{JK} \overline{P_J^n} + \frac{\Delta t}{2|\Omega_J|} \sum_K \alpha_{KJ} \overline{P_K^n} - \rho_0 c \frac{\Delta t}{2|\Omega_J|} \sum_K (\lambda_{JK} \overline{\mathbf{u}_J^n} + \lambda_{KJ} \overline{\mathbf{u}_K^n}) \cdot \mathbf{n}_{JK} \\ \overline{\mathbf{u}_j^{n+1}} = \overline{\mathbf{u}_j^n} - \frac{\Delta t}{2|\Omega_J|} \sum_K (a_{JK} \overline{\mathbf{u}_J^n} - a_{KJ} \overline{\mathbf{u}_K^n}) - \frac{\Delta t}{2|\Omega_J|} \sum_K ((b_{JK} \overline{\mathbf{u}_J^n} - b_{KJ} \overline{\mathbf{u}_K^n}) \cdot \mathbf{n}_{JK}) \mathbf{n}_{JK} \\ - \frac{\Delta t}{2|\Omega_J| \rho_0 c} \sum_K (\beta_{JK} \overline{P_J^n} + \beta_{KJ} \overline{P_K^n}) \mathbf{n}_{JK} \end{cases} \quad (29)$$

$$\begin{cases} \alpha_{JK} = c \|\mathbf{S}_{JK}\| \max(0, 2M_{JK}, M_{JK} + \Psi_{JK}^u) \\ \lambda_{JK} = c \|\mathbf{S}_{JK}\| \max(0, \min(2, 1 + \Psi_{JK}^P)) \\ \beta_{JK} = c \|\mathbf{S}_{JK}\| \max(0, \min(2, 1 + M_{JK} \Psi_{JK}^u)) \\ b_{JK} = c \|\mathbf{S}_{JK}\| \max(0, \Psi_{JK}^P - |M_{JK}|) \\ a_{JK} = c \|\mathbf{S}_{JK}\| \max(0, 2M_{JK}) \end{cases} \quad (30)$$

Here index  $JK$  refers to the left of the interface  $A_{JK}$  and index  $KJ$  to the right of the same interface. Note that  $M_{KJ} = -M_{JK}$ .

Another important condition for the solver is to remain stable for all Mach numbers. More precisely, we look for a strong stability condition given by the positivity of the scheme: the linear scheme (29) is positive if and only if all its constant coefficients are positive. Finding this conditions is not straightforward because the upwind approximation for the pressure (resp. velocity) in (29) is composed of a pressure (resp. velocity) term plus a coupled term with velocity (resp. pressure).

To circumvent this difficulty, (29) is rewritten in terms of the acoustic pseudo-eigenfunctions  $\Phi(\mathbf{k}) = P + \rho c \mathbf{u} \cdot \mathbf{k}$ , with  $\|\mathbf{k}\| \leq 1$ . Under the assumption that there exists a direction  $\mathbf{k}$  which cancels out the coupling terms in Eqs. (29), the positivity of the scheme can be derived by considering only the non-coupled coefficients of the scheme.

This leads, on the one hand to the following conditions on  $\Psi_{JK}^u$  and  $\Psi_{JK}^P$

$$\begin{cases} \Psi_{JK}^u \geq 1 \\ \Psi_{JK}^P \geq \min(1, |M_{JK}|) \end{cases} \quad (31)$$

which finally gives

$$\begin{cases} \Psi_{JK}^u \geq 1 \Rightarrow \Psi_{JK}^u = 1 \text{ (no recentering required on the velocity)} \\ \min(1, |M_{JK}|) \leq \Psi_{JK}^P \leq 1 \end{cases} \quad (32)$$

On the other hand, a stability condition on the time step  $\Delta t$  is obtained for the first-order Godunov scheme:

$$\Delta t \leq \tau_1 = \frac{2\Omega_J}{\sum_K (c \|\mathbf{S}_{JK}\| \max(0, 2M_{JK}, M_{JK} + 1) + c \|\sum_K \mathbf{S}_{JK} \max(0, \min(2, M_{JK} + 1))\|)} \quad (33)$$

We observe that conditions (32) obtained for the present recentering functions are coherent with other recentering procedures proposed in the litterature. Rieper applies the recentering function  $\Psi^P = \min(1, |M_{JK}|)$  to the Roe scheme [32]. Dellacherie also recenter the pressure gradients in the Godunov scheme in his so-called All Mach scheme [36].

In addition to the recentering function  $\Psi_0^P(M_{JK}) = \min(1, |M_{JK}|)$ , another function that tends continuously to 1 for  $M_{JK} = 1$  and verifies condition (32) has been tested:

$$\Psi_1^P(M_{JK}) = \frac{1}{1 - \min(1, |M_{JK}|) + \min(1, |M_{JK}|)^2} \quad (34)$$

The function  $\Psi_1^P$  is used in the present work within a Godunov-type solver using a MUSCL approach (see Section 6).  $\Psi_0^P$  and  $\Psi_1^P$  are represented in Figure 4.1. Note that the condition on pressure of the system (32) imposes that the pressure recentering function is above the blue curve in Figure 4.1 for  $M_{JK} \in [0, 1]$ .

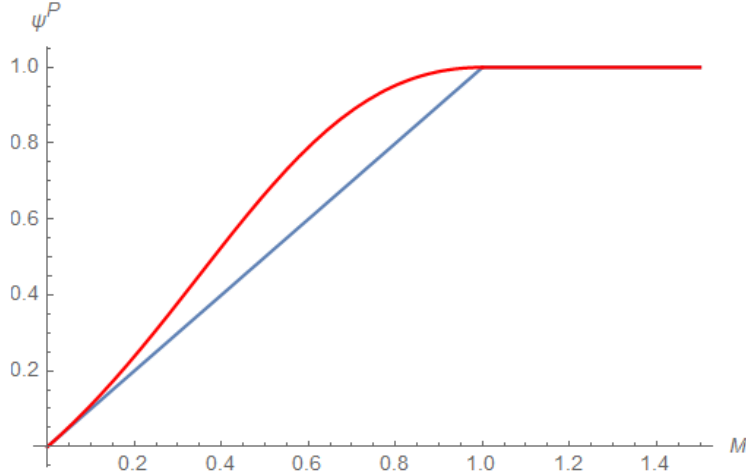


Figure 3: Representation of the functions  $\Psi_0^P$  (blue curve) and  $\Psi_1^P$  (red curve) for  $M_{JK} \in [0, 1.5]$

## 5 Near-wall discretization

### 5.1 Numerical strategy

In this part, the 1-exact and 2-exact reconstruction schemes presented in Section 2 are modified by enriching the reconstruction stencil and adapting the successive-corrections procedure. We will assume here that a Dirichlet boundary condition  $q_D(\mathbf{x} \in \partial\Omega)$  is prescribed at the wall. Other types of boundary conditions and strategies for boundary conditions approximation will be discussed in part 5.2.

The baseline solver of FLUSEPA does not take into account the wall in the polynomial reconstruction of the solution variables (the parameter  $\beta$  introduced in Section 2 is set to 0). The corresponding stencils used respectively for the second and third-order schemes for a boundary cell  $\Omega_J$  are shown in Figure 1.

To account for the wall contribution in the approximation of the derivatives, we introduce a ghost cell  $\Omega_W$  which corresponds to the wall boundary condition of the cell  $\Omega_J$ : it is not an average quantity but is calculated as a pointwise value in our methodology. Let  $s^*(J) = s(J) \cup \Omega_W$  be the extended neighbourhood of  $\Omega_J$ . Note that  $s^*(J) = s(J)$  when  $\Omega_J$  is inside the domain.

To build a second-order polynomial representation of the variable  $q$  that uses the boundary conditions, the Quasi-Green gradient must be extended: as in Eq. (7), we want

$$\iint_{A_{JW}} q \mathbf{n} dS = (\beta_W q(\mathbf{x}_W) + (1 - \beta_W) \bar{q}_J) \mathbf{A}_{JW} + \mathcal{O}(h^m) \mathbf{A}_{JW} \quad (35)$$

If we perform a Taylor expansion of the Dirichlet function *at any point of the wall face*  $\mathbf{x}_W \in A_{JW}$  in the integral  $\iint_{A_{JW}} q \mathbf{n} dS$ , we obtain a relation of the form of Eq. (35) with  $\beta_W = 1$ . Moreover, when the wall face is flat and  $\mathbf{x}_W$  is the center of gravity of the face, the approximation is second-order accurate ( $m = 2$ ) and the Green integral is consistent even without the correction matrix  $M_1^*(J)$ . On general grids,

however, this integral is only first-order accurate ( $m = 1$ ) and thus no longer consistent with the Green Gauss method. However, by nature of the Quasi-Green approach, the consistency of the overall gradient operator will be restored thanks to the simple correction matrix  $M_1(J)$ , if this matrix is corrected accordingly, giving a matrix  $M_1^*(J)$  that satisfies the 1-exactness consistency condition of Eq. (9):

$$M_1^*(J) = \frac{1}{|\Omega_J|} \sum_{K \in s^*(J)} \beta_K \mathbf{A}_{JK} \otimes (\mathbf{x}_K - \mathbf{x}_J), \text{ with } \beta_W = 1 \quad (36)$$

In the end, the enriched 1-exact gradient operator  $\mathcal{D}_1^{*(1)}$  is

$$\mathcal{D}_1^{*(1)} [\bar{q}]_J = M_1^{*-1}(J) \frac{1}{|\Omega_J|} \sum_{K \in s^*(J)} (\beta_K \bar{q}_K + (1 - \beta_K) \bar{q}_J) \mathbf{A}_{JK}. \quad (37)$$

with the notation  $\bar{q}_W = q_W$ .

To build a second-order polynomial reconstruction of the solution variables, the strategy is not as straightforward. Indeed, as can be seen in Figure 1 (b), the Quasi-Green operator  $\mathcal{D}_1^{*(1)} [\bar{q}]_J$  can not be applied twice since gradients in the neighbourhood of  $\Omega_J$  are missing.

We apply the enriched gradient operator and its associated correction matrix whenever possible, and keep the baseline approximation otherwise. With this choice, the initial inconsistent approximation of the second derivatives is obtained by applying the original 1-exact operator  $\mathcal{D}_1^{(1)}$  to the modified operator  $\mathcal{D}_1^{*(1)}$ :

$$\mathcal{D}_0^{*(2)} [\bar{q}]_J = \mathcal{D}_1^{(1)} \left[ \mathcal{D}_1^{*(1)} [\bar{q}]_J \right]_K \quad (38)$$

The correction matrix  $M_2(J)$  is modified in a similar way and a matrix  $M_2^*(J)$  is derived.

Then, the geometrical matrices  $(H_1(J))_{i \in \{1,3\}}$  of Eq. (15) giving the truncation error between the exact gradient and its 1-exact representation are changed into  $(H_1^*(J))_{i \in \{1,3\}}$  by adding a wall contribution where  $\beta_W = 1$  and taking the volume moments for cell  $\Omega_W$  null.

This strategy to improve the accuracy of the  $k$ -exact reconstruction in boundary cells can be theoretically perform for any order of exactness  $k$  by applying the original derivative operator successively ( $\mathcal{D}_1^{*(1)}$  is only used for the first step of the composition). However, one critical requirement must be satisfied for the strategy to be consistent : for a  $k$ -exact reconstruction, the boundary value  $q(\mathbf{x}_W)$  must be known at least to the order  $k + 1$ .

## 5.2 Boundary conditions

In the numerical strategy presented in part 5.1, we assumed that a Dirichlet condition was prescribed at the wall. In practice, multiple situations can happen for a variable  $q$ : imposed value at the wall (Dirichlet boundary condition), imposed gradient (Neumann boundary condition) or no information available at the wall. When curvature is taken into account, a specific physical boundary condition can be derived for the pressure in the Euler case, which consists in using the normal momentum equation verified for the Euler equations at the wall [37]:

$$\frac{\partial P}{\partial n}|_W = -\frac{\rho u_{tan}^2}{R} \quad (39)$$

with  $R$  the local radius of curvature of the wall face (which depends on the tangential velocity at the wall point and on the corresponding normal as explained in Section 3) and  $u_{tan}$  the tangential velocity magnitude.

As was said before, an essential requirement for the strategy of part 5.1 to be consistent is that the boundary value  $q(\mathbf{x}_W)$  is known at least to the  $k + 1^{th}$  order for a  $k$ -exact reconstruction scheme.

If a Dirichlet boundary function is given at the wall, we can directly use it to enforce the value  $q(\mathbf{x}_W)$ .

In the case for which nothing is known about the variable at the wall (for instance for the temperature in the Euler case), then one can only rely on the extrapolation from the inside of the domain. A Taylor expansion is performed to the required order of accuracy, in which the derivatives approximations at point  $\mathbf{x}_j$  at the previous time are used:

$$\mathbf{q}_{\mathbf{W}_o}^n = \bar{\mathbf{q}}_J^n + \sum_{l=1}^k \frac{1}{l!} \mathcal{D}_{k-1}^{*(l)n-1} [\bar{\mathbf{q}}]_J \cdot (\mathbf{x}_{\mathbf{W}} - \mathbf{x}_j)^{\otimes l} + \mathcal{O}(h^{k+1}) \quad (40)$$

where  $n$  is the current time. This method is acceptable for steady cases, but is not suitable for general unsteady cases. If the flow is unsteady, an assumption on time evolution of the wall values should be added to make the method consistent in time. The simplest condition to begin with is to enforce  $\frac{dq}{dt}|_i = \frac{dq}{dt}|_W$  to correct the wall value. Since only steady cases are considered in the following, this strategy has not been implemented in the present paper.

Assume now that a Neumann condition  $\frac{\partial q}{\partial n}(\mathbf{x} \in \partial\Omega) = \mathbf{D}^{(1)}\mathbf{q}(\mathbf{x}) \cdot \mathbf{n}(\mathbf{x})$  is prescribed at the boundary. We choose to calculate an equivalent fictitious value at the wall  $q_W^{fict}$  to fall back into the Dirichlet case. This way multiple definitions of the correction matrices are avoided: such a method would be possible but cumbersome and costly, and even more as the order of the reconstruction increases. An additional constraint in this situation is to have a single definition of the wall point. Since any point can be chosen in the Dirichlet case to get consistency with the  $M_1^*(J)$  matrix (see part 5.1), we choose the point  $\mathbf{x}_{\mathbf{W}} = \mathbf{x}_{\mathbf{N}}$  whose corresponding normal vector to the local surface is colinear to  $\mathbf{x}_{\mathbf{N}} - \mathbf{x}_j$ .

For a  $k$ -exact reconstruction scheme, the fictitious value  $q_W^{fict}$  must be calculated to the  $k^{th}$  order of accuracy. A Taylor expansion to the  $k^{th}$  order is performed. Since only the gradient is known at the wall, the other derivatives are taken at the previous time and projected in the local normal direction. Thus, a correction of the spatial value in time would be necessary for an unsteady configuration as was explained before.

The last situation is the case for which the boundary condition on a variable is known partially. Here, a strategy based on a Taylor expansion using the derivatives at the previous time is again performed, along with an extrapolation for the unknown part. This can be applied for example to the slip condition in the Euler case, where a Dirichlet-type condition is prescribed for the normal velocity, but no information is given on the tangential velocity.

## 6 Numerical results

### 6.1 Inviscid flow past a smooth Gaussian bump

To assess the models presented in the present article, we first consider an inviscid flow within a channel with a smooth Gaussian bump. The inflow Mach number is  $M = 0.5$  and the inlet flow angle is equal to 0. Left and right boundaries are respectively a subsonic inflow and a subsonic outflow (with imposed pressure), and the upper and lower boundaries are slip walls. Entropy, which should be constant in the flow field, is used as an indicator of the quality of the simulation since the analytical solution is unknown.

Figure 4 compares the entropy error for the 2-exact reconstruction scheme on a mesh having 80 wall faces along the bump. Spurious entropy generation is observed downstream of the bump, which is significantly reduced when adding the curvature model. In the rest of the domain where curvature is smaller, entropy is already correctly computed by the baseline method.

A mesh convergence study is carried out for the entropy error, using grids of 400, 1600, 6400, 25600 and 102400 cells, corresponding respectively to 40, 80, 160, 320, and 640 wall faces along the bump. Results are provided for the 1-exact and 2-exact reconstruction schemes, by comparing the baseline solver, the solver with curved boundaries, and the solver with curved boundaries and an enriched stencil at the wall.

Grid convergences for the 1-exact and 2-exact reconstruction schemes are shown in Figure 5 and 6 respectively.

For the scheme with 1-exact reconstruction, we see that the convergence slope when adding the curvature model to the scheme increases compared to using the unmodified scheme. However, the entropy error reduction is low. This is not surprising: as it was stressed before, the spatial error introduced when approximating curved surfaces with flat faces is of order 2. Yet, the approximation of the boundary should at least represent the real boundary with the same order of accuracy as the discretization scheme [10]. Here the original scheme with 1-exact reconstruction exhibits a convergence of order 2 at most, as can be seen in Figure 5. Even if the Bézier patches approximate the wall with third-order accuracy, the gain is expected to be small when

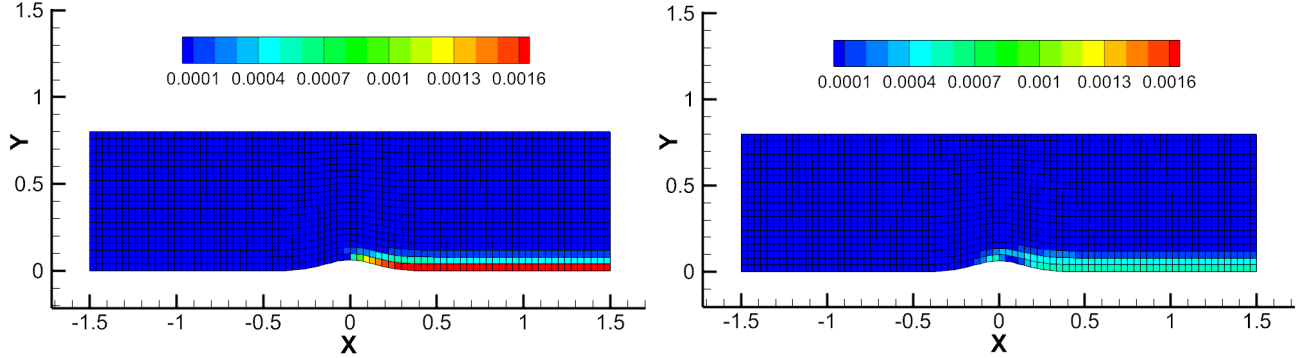


Figure 4: Inviscid Gaussian bump: entropy error generated downstream of the bump with the 2-exact scheme (a) with no modification; (b) with the wall curvature model

this only improvement is used in the solver.

When using the model with extended stencil in boundary cells along with curved walls, much larger improvements are obtained: the entropy error drops and the convergence slope is again increased. The information at the wall is accurate enough thanks to the inclusion of curvature and of a proper handling of boundary conditions (even if the information available at the wall for the Euler equations is limited), and is used consistently to calculate a 1-exact approximation of the gradient.

For the scheme with 2-exact reconstruction, satisfying results are obtained with the curvature model, which approximates the physical surface with a spatial error of order 3. The entropy error is reduced and more importantly, the convergence slope is significantly increased with this model (getting closer to third order in  $L_2$  norm).

In Figure 6, the error convergence is also reported with respect to the  $L_\infty$  norm, corresponding to the maximum local error in the domain. Accuracy improvements are even bigger in this norm, confirming the importance of using a curvature model to enhance the scheme accuracy near curved walls, where the error is preponderant.

When considering the curvature model coupled with the parabolic reconstruction with a more symmetrical stencil in boundary cells, no significant gain is observed. This is due to the fact that the boundary information in Euler is quite limited (a lot of quantities must be extrapolated) and is thus not sufficient to improve the overall parabolic reconstruction of the solution, contrary to the 1-exact scheme for which the first-order approximate gradients are significantly improved.

## 6.2 Subsonic flow around a circular cylinder

The two-dimensional inviscid test case of the flow around a circular cylinder is chosen to validate our low-Mach model. The advantage of this case is that an analytical solution is available in the incompressible regime, given by the well-known potential flow around a circular cylinder:

$$\begin{cases} u_{r,ref}(r, \theta) = U_\infty \left(1 - \frac{r_0^2}{r^2}\right) \cos(\theta) \\ u_{\theta,ref}(r, \theta) = -U_\infty \left(1 + \frac{r_0^2}{r^2}\right) \sin(\theta) \end{cases} \quad (41)$$

$$P_{ref}(r, \theta) = P_\infty + \frac{1}{2} \rho U_\infty^2 \left(2 \frac{r_0^2}{r^2} \cos(2\theta) - \frac{r_0^4}{r^4}\right) \quad (42)$$

where  $\mathbf{u}_\infty = U_\infty \mathbf{e}_x$  and  $P_\infty$  are the freestream velocity and pressure, and  $r_0$  is the radius of the cylinder.

The computational domain is  $\Omega = [r_0, r_1] \times [0, 2\pi]$ , with  $r_0 = 0.5$  and  $r_1 = 5$ . Simulations are first performed on a fixed mesh of 7500 cells (50 cells in the radial direction, 150 in the azimuthal direction), composed of a far field and of a slip wall boundary condition for the cylinder. Four different Mach numbers approaching the incompressible limit are studied:  $M = 10^{-1}$ ,  $10^{-2}$ ,  $10^{-3}$  and  $10^{-4}$ . The incoming velocity  $U_\infty$  is set to  $U_\infty = Mc$ , with  $c$  the speed of sound.

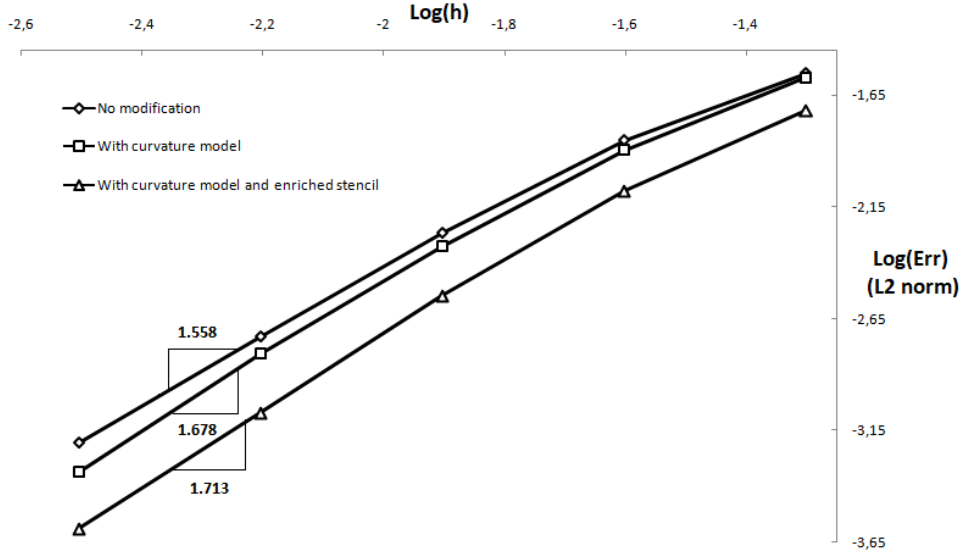


Figure 5: Inviscid flow past a bump: mesh convergence of the  $L_2$  norm of entropy error on the bump test case with the different models, for the 1-exact reconstruction scheme

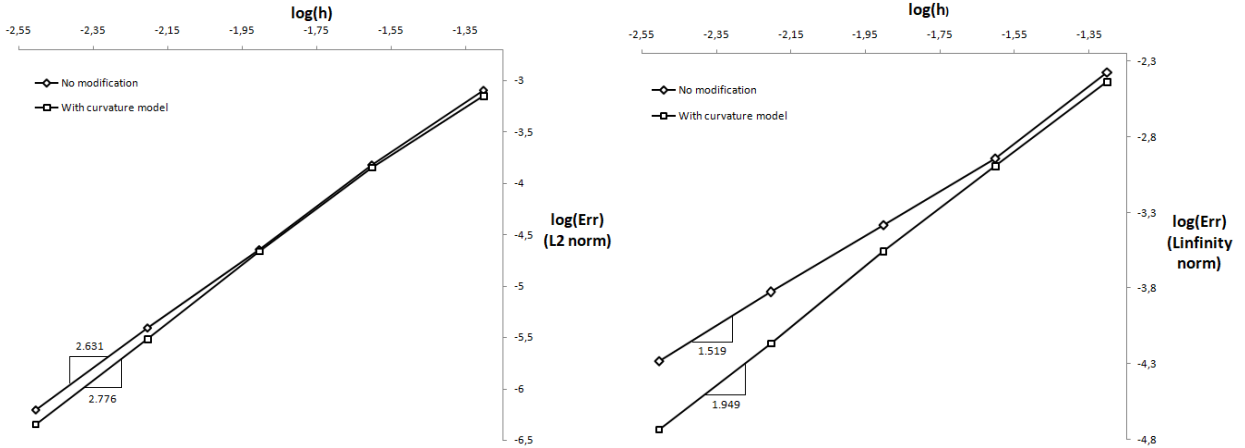


Figure 6: Inviscid flow past a bump: mesh convergence of the entropy error, 2-exact reconstruction scheme. (a)  $L_2$  norm; (b)  $L_\infty$  norm

The  $L_2$  norm of the pressure error  $\delta P = P - P_{ref}$  is investigated for several wall treatments: baseline solver, solver with low-Mach recentering, solver with curvature model for the wall faces, and solver with both curvature and low-Mach recentering. The results are reported for the 1-exact scheme in Table 1 and for the 2-exact scheme in Table 2. In order to take into account the proximity to the incompressible regime when comparing each simulation to the analytical solution,  $\delta P$  is scaled by  $\rho U_\infty^2$ , instead of being normalized by  $P_{ref}$  as it is generally done (see [32] for instance).

When using the 1-exact reconstruction scheme (Table 1), we see that the baseline solver gives acceptable results at  $M = 10^{-1}$  for the pressure error, similar to the one obtained by using the low-Mach correction.

However, for  $M = 10^{-2}$  or lower, the baseline scheme error increases as shown in Figures 8 and 9. Moreover, the pressure error do not converge well at  $M = 10^{-4}$ .

Introducing the low-Mach correction improves the results significantly, both in terms of accuracy and of convergence. The error of the corrected scheme is several orders of magnitude lower than the baseline one

Ma	BS	BS + LM	BS + C	BS + LM + C
$10^{-1}$	$1.12 \times 10^{-4}$	$1.86 \times 10^{-4}$	$7.53 \times 10^{-5}$	$7.96 \times 10^{-5}$
$10^{-2}$	$2.33 \times 10^{-3}$	$1.52 \times 10^{-4}$	$2.3 \times 10^{-3}$	$4.82 \times 10^{-5}$
$10^{-3}$	$1.08 \times 10^{-1}$	$2.31 \times 10^{-4}$	$9.32 \times 10^{-2}$	$6.53 \times 10^{-5}$
$10^{-4}$		$2.26 \times 10^{-4}$		$5.74 \times 10^{-5}$

Table 1: Pressure error  $\delta P$  scaled with  $\rho U_\infty^2$ , using the 1-exact scheme. BS = Baseline Solver, LM = Low-Mach recentered scheme, C = Curvature model, gray cell : did not converge well.

Ma	BS	BS + LM	BS + C	BS + LM + C
$10^{-1}$	$3.44 \times 10^{-5}$	$3.46 \times 10^{-5}$	$3.33 \times 10^{-5}$	$3.38 \times 10^{-5}$
$10^{-2}$	$1.65 \times 10^{-4}$	$1.19 \times 10^{-5}$	$1.62 \times 10^{-4}$	$1.12 \times 10^{-5}$
$10^{-3}$	$2.72 \times 10^{-3}$	$2.51 \times 10^{-5}$	$2.67 \times 10^{-3}$	$2.45 \times 10^{-5}$
$10^{-3}$	$2 \times 10^{-2}$	$3.37 \times 10^{-5}$	$1.99 \times 10^{-2}$	$3.34 \times 10^{-5}$

Table 2: Pressure error  $\delta P$  scaled with  $\rho U_\infty^2$ , using the 2-exact scheme. BS = Baseline Solver, LM = Low-Mach recentered scheme, C = Curvature model, gray cell : did not converge well.

for  $M = 10^{-3}$  and  $M = 10^{-4}$ .

Levels of the rescaled pressure error with the recentered scheme remains the same for all considered Mach (see Table 1), which is an expected feature showing the ability of the recentering strategy to solve the low-Mach accuracy problem of our compressible solver. Indeed, with the choice of scaling  $\delta P$  with  $\rho U_\infty^2$ , an acceptable error is supposed to remain of the same order for all Mach numbers: when the Mach number decreases,  $(P - P_{ref})$  decreases (because we are closer to the incompressible regime) and  $U_\infty$  decreases too such that  $(P - P_{ref})$  is scaled by a smaller quantity (linked to the incompressible Bernoulli formulation): consequently  $\frac{P - P_{ref}}{\rho U_\infty^2}$  remains of the same order.

Similar behaviours are obtained for the 2-exact scheme (Table 2) with the low-Mach recentering scheme. In this case however, the baseline scheme is more accurate and introduces smaller errors even without low-Mach correction. As a consequence, the benefit of low-Mach recentering is less significant. Once again, we stress the importance of introducing the curvature correction in conjunction with high-order schemes. Curvature corrections not only reduce the overall error levels but also alleviate the checkerboard oscillations that can appear in the error [38].

Lastly, a mesh convergence study is made in Figure 7, for the 1-exact and 2-exact reconstruction schemes for a fixed Mach number of  $M = 10^{-3}$ , on three grids of respectively 456, 1850 and 7500 cells with the low-Mach scheme on the one hand, and with the low-Mach scheme coupled with the curvature model on the other hand. For the 1-exact reconstruction scheme, second order is retrieved, and the coupling of the low-Mach and curvature models yields to a slightly increase of the order of accuracy. For the 2-exact reconstruction scheme, third-order is retrieved. However, again, coupling the low-Mach with curvature models have only a slight effect on the overall accuracy of the simulation.

## 7 Conclusions

An improved treatment of the near wall regions is investigated for a family of  $k$ -exact Godunov-type schemes, with focus on the 1-exact and 2-exact reconstruction schemes.

Firstly, a high-order composite representation of the wall based on bicubic Bézier patches is incorporated into the solver. The computation of geometrical quantities is modified close to the wall to conform to the patches, notably the volume moments, surface moments and integration points essential to the reconstruction and to the flux integration.

Secondly, a recentering technique based on the normal Mach number is used to modify the Riemann solver used to calculate the convective fluxes. The scheme remains unchanged for Mach numbers above one and is recentered for Mach number lower than one, which makes the changes consistent with the original

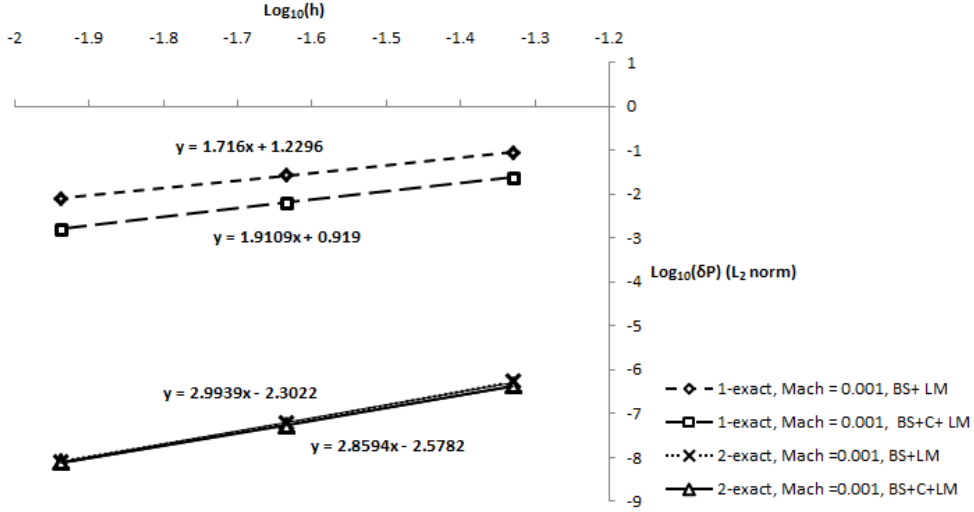


Figure 7: Mesh convergence study for the subsonic cylinder, at  $M = 10^{-3}$ , with  $\delta P$  scaled by  $P_{ref}$ . BS: Baseline solver, LM: Low-Mach recentered scheme, C: Curvature model

method.

Thirdly, a numerical strategy is presented to enrich the stencil with the boundary information in the reconstruction procedure. The flow variables are evaluated at a wall point  $\mathbf{x}_W$  whose normal is colinear to the direction  $\mathbf{x}_j - \mathbf{x}_W$  ( $\mathbf{x}_j$  being the boundary cell centroid). This allows to apply the same methodology to Dirichlet-type boundary conditions and to Neumann-type boundary conditions. In the latter case, a fictitious Dirichlet value is derived at the wall point by means of a Taylor expansion in the wall normal direction. For the 2-exact scheme, the approximate gradient operator with enriched stencil is applied only one time in the successive-corrections procedure, and correction matrices are modified in a similar way. In all cases, flow variables have to be determined at the wall point with at least the same order of accuracy as the reconstruction.

The proposed improved schemes are assessed against to inviscid flow problems, namely, the flow in a channel with a Gaussian bump and the flow past a circular cylinder.

The results show that, in all cases, accounting for wall curvature improves the solution accuracy significantly. The benefit is larger for the 2-exact scheme, which includes more geometrical information. Conversely, low-Mach corrections are more influential for the more dissipative 1-exact scheme, although improvements are observed at all orders. Enriching the reconstruction stencil close to the wall also leads to solution improvements, but less significant than the two former corrections, especially for the 2-exact scheme.

As future work, the approach will be applied to viscous flows, with focus on the near-wall treatment of the viscous fluxes.

## References

- [1] T. J. Barth and P. O. Frederickson. Higher order solution of the euler equations on unstructured grid using quadratic reconstruction. *AIAA Paper 90-0013*, 1990.
- [2] T. J. Barth. Recent developments in high order k-exact reconstruction on unstructured meshes. *AIAA Paper 93-0668*, 1993.
- [3] P. Vankeirsbilck and H. Deconinck. Higher order upwind finite volume schemes with eno-properties for general unstructured meshes. *AGARD report*, 1992.
- [4] C. Ollivier-Gooch and M. Van Altena. A high-order accurate unstructured mesh finite-volume scheme for the advection-diffusion equation. *Journal of Computational Physics*, 182(2):729–752, 2002.
- [5] D. Caraeni. Unstructured-grid third-order finite volume discretization using a multistep quadratic data-reconstruction method. *AIAA Journal*, 4:808–817, 2010.
- [6] F. Haider, P. Brenner, B. Courbet, and J. P. Croisille. Efficient implementation of high order reconstruction in finite volume methods. *Finite Volumes for Complex Application VI-Problem & Perspectives*, Springer, 4:553–560, 2011.
- [7] Pont, G. and Brenner, P. and Cinnella, P. and Maugars, B. and Robinet, J. C. Multiple-correction hybrid k-exact schemes for high-order compressible rans-les simulations on fully unstructured grids. *Journal of Computational Physics*, 350:45–83, 2017.
- [8] P. Brenner. Unsteady flows about bodies in relative motion. *Proceedings of the First AFOSR Conference on Dynamic Motion CFD: New Brunswick, New Jersey*, 1996.
- [9] J. Giesselmann and T. Muller. Geometric error of finite volume schemes for conservation laws on evolving surfaces. *Numerische Mathematik*, 128(3):489–516, 2014.
- [10] C. Ollivier-Gooch, A. Nejat, and K. Michalak. Obtaining and verifying high-order unstructured finite volume solutions to the euler equations. *AIAA Journal*, 47(9):2105–2120, 2009.
- [11] D. Sun F. Qu. Investigation into the influences of the low-speed flows’ accuracy on rans simulations. *Aerospace Science and Technology*, 70:578–589, 2017.
- [12] P. Bézier. *The mathematical basis of the UNISURF CAD system*. Butterworths, 1986.
- [13] G. Farin. *Curves and Surfaces for Computer-Aided Geometric Design - A practical guide*. Academic Press, Elsevier, 1993.
- [14] H. Borouchaki. Bshape, interpolant quasi g1 d’une surface discrÃte : descriptif technique. Unpublished report, 2015.
- [15] G. Pont, D. Puech, M. Jubera, and P. Brenner. Cfd modeling of the ariane 6 space launch from ground to space. *8th European Symposium on Aerothermodynamics for Space Vehicles*, 2015.
- [16] A. Limare, P. Brenner, and H. Borouchaki. Toward a high-order mesh adaptation strategy for unsteady flows on overlapping grids in a finite-volume framework. *46th AIAA Fluid Dynamics Conference, AIAA Aviation Forum*, 2016.
- [17] K.Heun. Neue methoden zur approximativen integration der differentialgleichungen eincr unablaingigen ver’anderliehen.
- [18] M.H. Schultz Y. Saad. Gmres: A generalized minimal residual algorithm for solving nonsymmetric linear systems. *SIAM Journal on Scientific and Statistical Computing*, 7, 1986.
- [19] A. Jalali, M. Sharbatdar, and C. F. Olliver-Gooch. Accuracy analysis of unstructured finite volume discretization schemes for diffusive fluxes. *Computer and Fluids*, 101:220–232, 2014.
- [20] Q. Wang, Y. X. Ren, and W. Li. Compact high order finite volume method on unstructured grids i: Basic formulations and one-dimensional schemes. *Journal of Computational Physics*, 314:863–882, 2016.
- [21] D. J. Mavriplis. Revisiting the least-squares procedure for gradient reconstruction on unstructured meshes. *16th AIAA Computational Fluid Dynamics Conference*, 2003.
- [22] F. Haider, P. Brenner, B. Courbet, and J. P. Croisille. Applications of efficient parallel k-exact finite volume reconstruction on unstructured grids. *ECOMAS Conference in Barcelona, Spain*, 2014.
- [23] B. Van Leer. Towards the ultimate conservative difference scheme. v. a second-order sequel to godunov method. *Journal of Computational Physics*, 32:101–136, 1979.
- [24] D. J. Walton and Meek D. S. A triangular g1 patch from boundary curves. *Computer-Aided Design*, 28(2):113–123, 1996.
- [25] G. Volpe. Performance of compressible flow codes at low mach numbers. *AIAA journal*, 31, 1993.
- [26] S. Dellacherie, J. Jung, P. Omnes, and P. Raviart. Construction of modified godunov type schemes

- accurate at any mach number for the compressible euler system. *Mathematical Models and Methods in Applied Sciences*, 2015.
- [27] F. Rieper S. Dellacherie, P. Omnes. The influence of cell geometry on the godunov scheme applied to the linear wave. *Journal of Computational Physics*, (229):5315–5338, 2010.
  - [28] G. Bader F. Rieper. The influence of cell geometry on the accuracy of upwind schemes in the low mach number regime. *Journal of Computational Physics*, 228:2918–2933, 2009.
  - [29] B. Nkonga H. Guillard. On the behaviour of upwind schemes in the low mach number limit : a review. *Handbook of numerical analysis Elsevier, Chapter 8*, 18, 2017.
  - [30] C. Viozat H. Guillard. On the behavior of upwind schemes in the low mach number limit. 28:63–86, 1999.
  - [31] A. Murrone H. Guillard. On the behavior of upwind schemes in the low mach number limit. ii : Godunov type schemes. 33:655–675, 2004.
  - [32] F. Rieper. A low-mach number fix for roe’s approximate riemann solver. *Journal of Computational Physics*, 230:5263–5287, 2011.
  - [33] E. Turkel. Preconditioned methods for solving the incompressible and low speed compressible equations. 1987.
  - [34] J. C. Boniface. Rescaling of the roe scheme in low-mach number flow regions. *Journal of Computational Physics*, 328:177–199, 2017.
  - [35] E. F. Toro. *Riemann Solvers and Numerical Methods for Fluid Dynamics : A Practical Introduction*. Verlag Springer, 2009.
  - [36] P. Omnes P. A. Raviart S. Dellacherie, J. Jung. Construction of modified godunov-type schemes accurate at any mach number for the compressible euler equations. *Mathematical Models and Methods in Applied Sciences*, 26(13), 2016.
  - [37] Dadone, A. Some solutions of the equations of flow of a viscous compressible fluid. *International Journal for Numerical Methods in Fluids*, 28:1093–1108, 1998.
  - [38] S. Dellacherie. Checkerboard modes and wave equation. *Proceedings of Algorithmy*, pages 71–80, 2009.

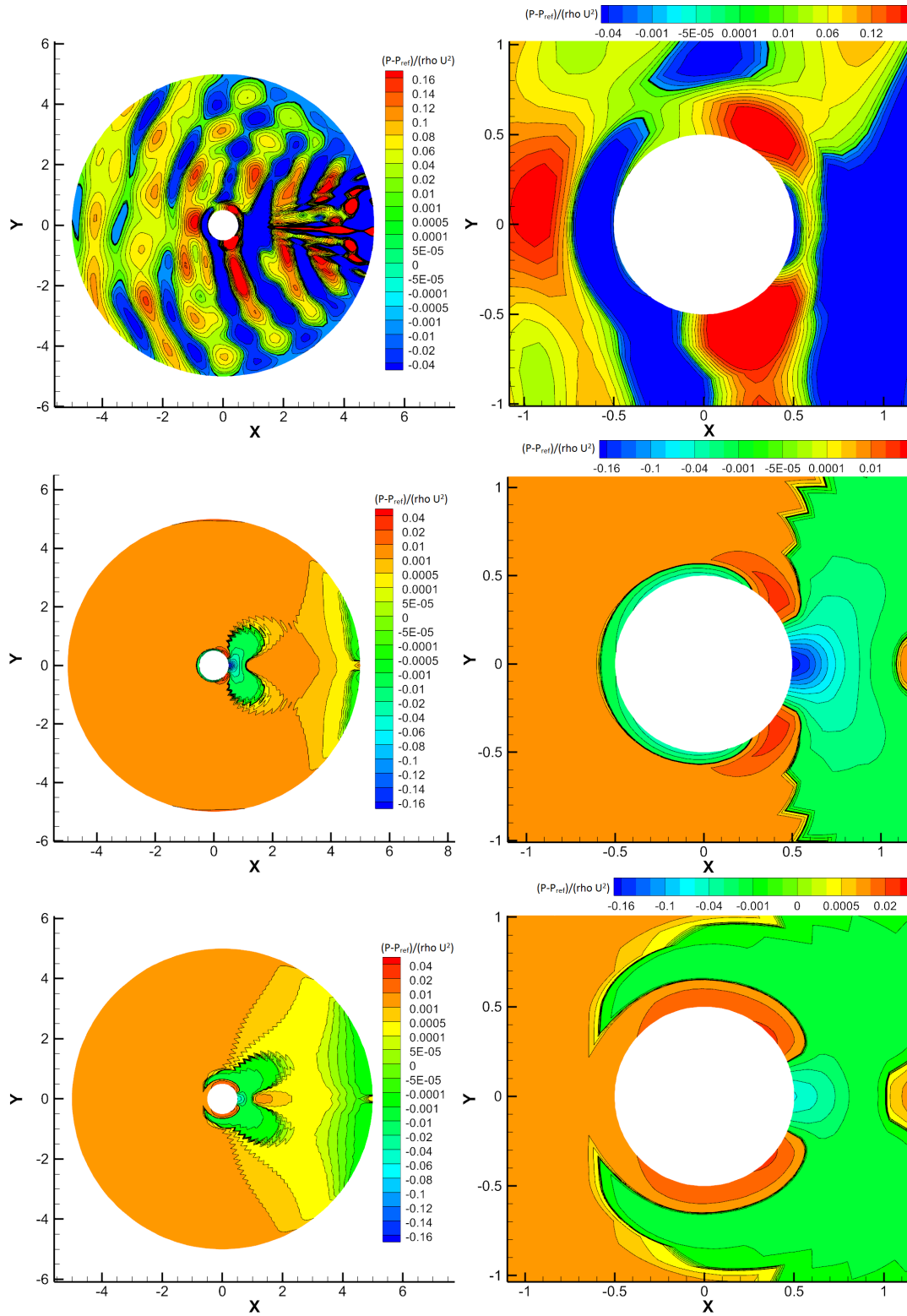


Figure 8: Pressure error levels and contours,  $M = 10^{-2}$ . Entire domain at the left, focus (zoom) on the cylinder at the right. Top : Baseline solver , middle : solver with low-Mach recentering , bottom : solver with low-Mach recentering and model of curvature.

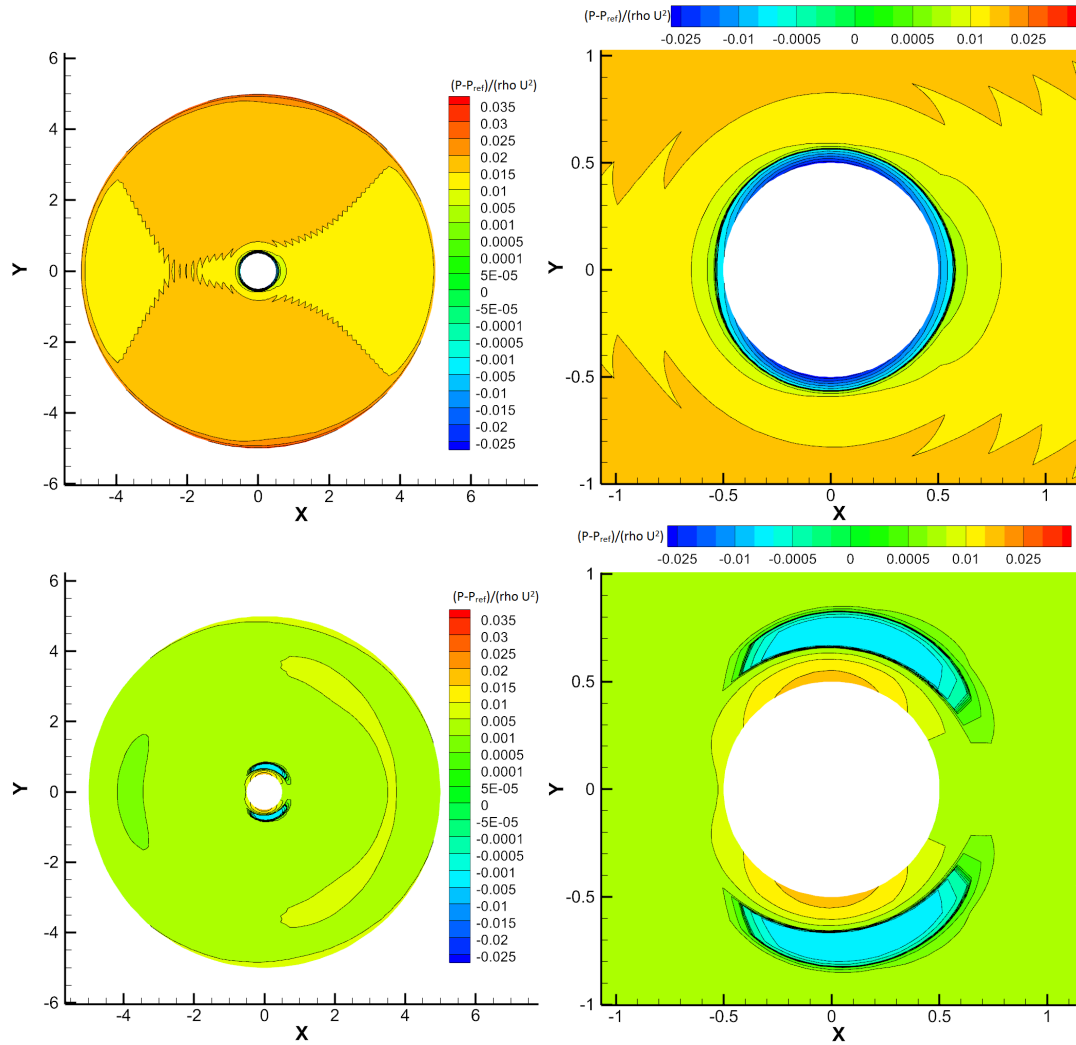


Figure 9: Pressure error levels and contours,  $M = 10^{-4}$ . Entire domain at the left, focus (zoom) on the cylinder at the right. Top : Baseline solver , middle : solver with low-Mach recentering , bottom : solver with low-Mach recentering and model of curvature.